Journal of Manufacturing Processes xxx (xxxx) 1–15

Contents lists available at ScienceDirect

Journal of Manufacturing Processes

journal homepage: www.elsevier.com/locate/manpro

Numerical modeling of *Ti-6Al-4V* alloy orthogonal cutting considering microstructure dependent work hardening and energy density-based failure behaviors

Guang Chen [a, *], James Caudill [b], Chengzu Ren [a], I.S. Jawahir [b]

[a] Tianjin University, Key Laboratory of Mechanism Theory and Equipment Design Ministry of Education, Tianjin 300354, People's Republic of China
[b] Institute for Sustainable Manufacturing (ISM), University of Kentucky, Lexington, KY, USA

ARTICLE INFO

Keywords:
Constitutive model
Finite element simulation
Cutting
Grain refinement
Energy density
Surface integrity

ABSTRACT

Numerical modeling of the cutting process provides an effective method to obtain the micro-scale and instantaneous process information which is difficult to be measured by experiments. A new microstructure (grain size) dependent work hardening plastic (JCM-ms) model was developed to characterize the effect of grain refinement on the cutting process. An energy density-based failure law was applied to control the chip formation and material removal mechanisms ahead of the cutting edge. Orthogonal cutting experiments with different edge radii and uncut chip thickness values for *Ti-6Al-4V* alloy were carried out to validate the finite element (FE) simulation results. The simulation results were thoroughly validated by the measured principal and thrust forces, segmented chip morphology, and the grain refinement within the machined surface layer. The distribution of grain refinement of the chips and machined surface agreed well with the experimental results. The positions of stagnation points with different edge radii and uncut chip thickness values were measured by the FE simulation results. The variation of surface morphology along the speed direction with larger edge radius is related to the variation of the stagnation points, which will affect the ratio of material being compressed to the machined surface by the tool, during the formation of the adiabatic shear band. The degree of the subsurface shear deformation determines the final distribution of the micro-hardness. Larger shear displacement at the top surface will lead to thicker layer of grain refinement. Residual stresses along the depth from machined surface are mainly related to the displacement normal to the machined surface. The height of the stagnation point is in proportion to the peak compressive stresses induced by the material flow ahead of cutting edge for different conditions. This work provides an effective method to characterize the forces, grain refinement and surface integrity for the orthogonal cutting of *Ti-6Al-4V* alloy.

1. Introduction

The metal cutting action involves complex thermo-mechanical loading processes, including large strain, high strain-rate, temperature and large gradients of the temperature and strain-rate. It is very difficult to characterize and investigate the material removal mechanism during the instantaneous cutting process. Finite element method (FEM) can be used to analyze the instantaneous information on variables such as stress, strain, strain-rate, temperature and the damage in high strain-rate deformation processes, including impact, stamping, cutting, etc. FEM has become a powerful methodology, which is widely applied in various industrial fields to calculate material deformation or damage, predict material and structural strength, vibration characteristics, etc. It can also predict material deformation across multiple length-scales, including macro, micro or sub-micro scale (0.1 μm ~ 1 μm).

For the cutting process, classical metal cutting theories are normally deduced according to experimental results, such as forces, temperature, chip morphology, as well as theoretically deduced based on assumptions. To further understand the fundamentals of the cutting process, the in-situ and ex-situ characterization of the cutting process should be concerned for the time-dependent cutting process [1,2]. Since the strain-rate in cutting deformation process is very high (10^4 s^{-1}-10^6 s^{-1}), cutting simulations with FEM provide an effective way to characterize the deformation mechanism for cutting at micro-scale.

Numerical modeling of metal cutting processes by FEM can be used to predict the macro-forces, chip morphology, tool wear, micro-

* Corresponding author.
E-mail address: guangchen@tju.edu.cn (G. Chen).

https://doi.org/10.1016/j.jmapro.2022.08.032
Received 12 June 2022; Received in revised form 10 August 2022; Accepted 18 August 2022
1526-6125/

material and mechanical behaviors [3]. Cutting simulation results are commonly calibrated by experimental forces or chip morphology, which are dependent on the thermo-mechanical behaviors, i.e., the flow stresses at various temperatures and loading strain-rates. Therefore, the material constitutive model used to characterize the relationship between the stress, strain, strain-rate as well as the temperature, is the critical factor which affects the accuracy of the FE model. To simulate the cutting process with FEM, the constitutive model should include both a plastic constitutive model, which controls the flow stress for the stage of plastic deformation, and a damage (or failure) model, which is used to control the failure behavior (i.e. the decrease of flow stress, during material removal).

The plastic constitutive models for high strain-rate deformation are mainly classified in two categories: the phenomenological models and so-called physically-based ones. The classical phenomenological Johnson-Cook (J-C) model was developed by Johnson and Cook in 1983 [4] to characterize the relationship between stress, strain and temperature for high-strain-rate deformation. It has been widely applied in high-strain-rate deformation simulations and is embedded in many FE commercial software packages. Besides, the Khan–Huang–Liang (KHL) models can characterize the plastic flow stress for different materials during the high strain-rate machining processes [5,6]. The parameters of the constitutive models are normally calibrated by quasi-static and high strain-rate mechanical tests. Note that material behaviors, including the work-hardening, strain rate hardening and thermal softening may vary with materials. For example, negative strain-rate sensitivity (SRS) and negative to positive SRS were observed for aluminum alloys [7,8], and the third type strain aging was observed for Q235B steel [9]. Overall, researchers have developed various models to characterize the conjoined effect of strain, strain-rate and temperatures for different materials and loading conditions. Based on the JC model, the TANH model [10] and a series of modified/extended JC models [11] were developed to characterize the strain softening effect and the interaction effects of flow softening, strain hardening and thermal softening in machining simulation of *Ti-6Al-4V* alloy. The morphologies of the segmented chips were accurately predicted by the developed models, due to the flow softening of the material along the shear band of the chips. Chen et al. [12] developed JCM and KHLM models to characterize the temperature dependent work hardening for *Ti-6Al-4V* alloy, and the models were applied to simulate the high strain-rate compression tests and segmented chip formation in orthogonal cutting with an energy density based failure law [13,14]. That is, two strategies can be employed in FE simulations to predict the segmented chip formation, i.e., plastic model with strain softening behavior and plastic model with damage or failure law.

The physically based models, e.g. Zerilli and Armstrong model [15], Mecking and Kocks model [16], were developed based primarily on the mechanisms of plastic deformation related with dislocation density, phase transformation or dynamic recrystallization (DRX). Viscoplastic self-consistent (VPSC) model was proposed to investigate the effects of the deformation history on crystallization texture evolution in the simulation of large strain extrusion machining process [17]. However, the material constants of the phenomenological and physically based models are normally "fitted" by the uniaxial stress-strain curves at various temperatures and strain-rates [18]. From a mathematical point of view, any model with a large numbers of material constants will be able to predict the responses for different conditions. Therefore, plastic models with high prediction accuracy and less parameters are widely used in industry considering the application efficiency.

In recent years, with the development of modeling technology of FE simulation, some physically-based cutting models were proposed to predict micro-scale material and mechanical characteristics such as grain size, dislocation density and micro-hardness [19]. Machining simulation employing Johnson–Mehl–Avrami–Kolmogorov (JMAK) model has been used for evaluation of dynamic recrystallization (DRX) induced grain size evolution [20]. Wang et al. [21] predicted the grain size and microhardness in high speed machining of *Ti-6Al-4V* alloy with a JC plastic model utilizing the Zener-Hollomon parameter and Hall-Petch grain boundary strengthening. Sadeghifar et al. [22] applied JC model and JMAK based DRX model to predict the average grain size in machining of *Ti-6Al-4V* alloy. Three series of JMAK constants were applied and the simulated results were compared with each other. Xu et al. [23] investigated the grain refinement for High Speed Machining (HSM) of *Ti-6Al-4V* using TANH plastic model and JMAK DRX model. The grain refinement in HSM of *Ti-6Al-4V* alloy was determined through FE and cellular automata (CA) methods. Although the JMAK DRX model was successfully applied in cutting simulations of *Ti-6Al-4V* alloy, the parameters of the model were fitted based on quasi-static hot compression tests. For example, the JMAK parameters obtained at the compression tests under the strain-rate range of 0.01–10 s^{-1} [24], were commonly applied in machining simulations of *Ti-6Al-4V* alloy [22,23,25]. Although the loading strain-rate was much lower than actual cutting conditions, it is very difficult to obtain the microstructure evolution in cutting experiments due to the limited loading duration at high-strain-rate conditions. Additionally, the afore-mentioned models predicted the grain size in the cutting process based on the evolution of the strain, strain-rate and temperature. However, the influence of grain refinement on the flow stress was not considered.

It has been widely reported that grain refinement can increase the strength, hardness and ductility [26,27]. In machining, grain refinement occurs in the machined surface layer, or within the adiabatic shear bands (ASB) of the segmented chips due to the high strain-rate (10^4 s^{-1}-10^6 s^{-1}) and large plastic strain (1–17) [2,28]. Therefore, to ensure modeling fidelity in high strain-rate deformation processes, it is necessary to consider the effect of grain refinement on the flow stress though modification of the defining constitutive modeling. Khan et al. [29] modified the KHL model by incorporating Hall-Petch relationship to characterize the grain size dependent yield stress of Split Hopkinson Pressure Bar (SHPB) tests for fully compacted nanocrystalline material. Similarly, different forms of Hall–Petch types were successfully to embedded in KHL and Khan–Liang–Farrokh (KLF) models to characterize the flow stresses at quasi-static and dynamic strain-rates for nanocrystalline and ultra-fine grained Cu and Al through uniaxial compressive loading [30,31]. Yadav et al. [32] developed a dynamic recrystallization related material model considering a coupled effects of JC and TANH models for micro-machining simulation of Ti-6Al-4V alloy. Jafarian et al. [33] modified the work hardening component of the JC model to consider the influence of grain refinement on the plastic flow stress for the cutting simulations of a nickel-based alloy. Umbrello et al. [34] considered the effect of grain refinement on the flow stress in simulations of dry and cryogenic machining of EBM *Ti-6Al-4V* alloy, and the predicted alpha lamellae thickness and nano-hardness agreed well with the experimental results. Additionally, some physically-based models which considered thermal stresses and a dislocation drag stress [35,36] were used to characterize the evolution of dislocation density and to predict the machining-induced grain size and micro-hardness. Melkote et al. [37] proposed a physically based model considering the microstructure evolution induced flow softening due to the inverse Hall–Petch effect in orthogonal cutting simulation of pure titanium. This kind of modeling methodology also considered the mathematical influence of microstructure on the macro-flow stresses. Additionally, to make the classification of the aforementioned models clearer, the typical modeling method and characteristics considering phenomenological, physically-based and the microstructure-based models are listed in Table 1.

Although many numerical models have been used to simulate the cutting process, due to the complex thermal-mechanical loading, there are still yet key factors that need to be further investigated: i) The effect of the microstructure evolution on cutting performance; ii) The separation or sacrificed layer used in cutting simulation models is difficult to obtain the accurate principal and thrust forces simultaneously, and is

Table 1
Typical constitutive models for modeling of cutting process.

	Constitutive models	Characteristics	Failure behaviors
Phenomenological models	Johnson-Cook (J-C) model [4]	High strain rate deformation considering the effects of strain, strain rate and temperature	
	Khan–Huang–Liang (KHL) model [5,6]	Considering the coupled strain and strain-rate effects on the work-hardening behavior	
	Models considering strain rate sensitivity (SRS) [7–9]	Considering the negative, negative to positive, or third type SRS	
	TANH model [10], Modified/extended JC models [11]	Considering strain softening, temperature dependent strain softening effects	
	JCM and KHLM Model [12]	Considering the temperature dependent work hardening behavior	
Physically-based Models	Zerilli and Armstrong model [15]	Considering mechanisms of plastic deformation related with dislocation density, phase transformation or dynamic recrystallization (DRX)	
	Mecking and Kocks model [16]		
	Viscoplastic self-consistent (VPSC) model [17]	Considering the effect of the deformation history on crystallization texture evolution	
	Johnson–Mehl–Avrami–Kolmogorov (JMAK) model [20]	Modeling the evaluation of DRX induced grain size evolution	
Models used for cutting simulation considering microstructure evolution	JC model and JMAK based DRX model [22]; TANH plastic model and JMAK DRX model & cellular automata (CA) method [23]	• Modeling of microstructure • Microstructure independent plastic model	• Cockroft-Latham's criterion • JC damage model with fracture energy • shear damage model
	DRX related material model considering a coupled effect of JC and TANH models [32], grain size related JC model [33] and strain softening model [34]	• Modeling of microstructure • Microstructure dependent plastic model • Grain size related flow stress	
	Physically based model considering dislocation mechanism [35–37]	• Athermal, thermal and dislocation drag stresses related plastic behavior • Considering mobile dislocations based on Mecking and Kocks 's model [16]	• Flow softening related to inverse Hall–Petch effect

also difficult to simulate the material flow happened ahead of the cutting edge; iii) The traditional failure evolution criterion based on a failure strain normally leads to mesh dependence for the simulation results. iv) The surface integrity is difficult to predict using numerical models.

In this work, a numerical model for orthogonal machining of *Ti-6Al-4V* alloy is developed using a grain refinement dependent work hardening plastic constitutive model, along with an energy density-based failure law. The simulated results include the generated forces, chip and surface grain refinement, which are experimentally validated. The surface integrity, including the surface topography, micro-hardness and residual stresses will be investigated with different edge radii and uncut chip thickness values.

2. Material constitutive model

2.1. Plastic model

JC plastic model [4] has been widely applied in high strain-rate (10^2 s^{-1} to 10^6 s^{-1}) deformation-related processes, such as metal working or machining. The JC constitutive equation is defined as:

$$\sigma = (A + B\varepsilon^n)\left(1 + C\ln\dot{\varepsilon}^*\right)\left[1 - \left(\frac{T - T_r}{T_m - T_r}\right)^m\right] \quad (1)$$

where σ is the equivalent stress, $\dot{\varepsilon}^* = \dot{\varepsilon}/\dot{\varepsilon}_0$, ε and $\dot{\varepsilon}$ are the equivalent plastic strain and strain-rate, respectively. $\dot{\varepsilon}_0$ is the reference strain-rate. In this work, $\dot{\varepsilon}_0$ is defined as 0.01 s^{-1}. T_r and T_m are workpiece ambient (25 °C) and melting temperature (1660 °C for *Ti-6Al-4V* alloy), respectively. A, B, n, C and m are material parameters which are commonly determined by mechanical tests at various loading temperatures and strain-rates.

Note that the coupled effects of work hardening and temperature cannot be characterized by the JC model. Based on the high strain-rate SHPB test results, temperature dependent work hardening rate was observed for *Ti-6Al-4V* alloy [12]. the original JC model was modified by a temperature-dependent work hardening plastic (JCM) model which is given as

$$\sigma = \left[A + B\phi(T)(\varepsilon)^n\right]\left[1 + C\ln\left(\frac{\dot{\varepsilon}}{\dot{\varepsilon}_0}\right)\right]\left[1 - \left(\frac{T - T_r}{T_m - T_r}\right)^m\right] \quad (2)$$

$$\phi(T) = \left(\frac{T_0 - \frac{T}{2}}{T_0}\right)^{n_2} \quad (3)$$

where n_2 ($0 < n_2 < 1$) is an exponential coefficient, and T_0 is a critical temperature related to microstructure evolution. In this work, the range of T_0 is given as $450 < T_0 < 700$ °C, $0 < T < 2\,T_0$. The parameters of the JCM model for *Ti-6Al-4V* alloy are listed in Table 2.

2.2. Microstructure model

For thermo-mechanical deformation processes, generated dislocations will increase and accumulate to a certain strain when DRX nucleate and grow up near the grain boundaries, twin boundaries and deformation bands [24].

DRX will be activated when the plastic strain reaches a critical strain $\varepsilon_c = a_2\varepsilon_p$. The peak strain ε_p can be given defined [38] as.

Table 2
JCM model parameters for *Ti-6Al-4V* alloy [12].

A/MPa	B/MPa	n	C	m	n_2	T_0/°C
789.556	911.446	0.306	0.012	0.952	0.349	462.314

$$\varepsilon_p = a_1 d_0^{h_1} \dot{\varepsilon}^{m_1} \exp\left(Q_1/RT\right) + c_1 \tag{4}$$

where a_1, a_2, h_1, m_1 and c_1 are material constants, R is gas constant, Q_1 is current activation energy.

The recrystallized volume fraction, X_{DRX}, is characterized by the true strain, ε, according to the well-known Johnson–Mehl–Avrami–Kolmogorov (JMAK) model [39–41]

$$X_{DRX} = 1 - \exp\left[-\beta_d \left(\frac{\varepsilon - a_{10}\varepsilon_p}{\varepsilon_{0.5}}\right)^{k_d}\right] \tag{5}$$

where β_d and k_d are Avrami material constants, a_{10} is a material parameter, $\varepsilon_{0.5}$ is the strain with DRX volume fracture of 50 %, and it can be determined by an empirical model as

$$\varepsilon_{0.5} = a_5 d_0^{h_5} \dot{\varepsilon}^{m_5} \exp\left(Q_5/RT\right) + c_5 \tag{6}$$

where Q_5 is the activation energy for recrystallization, and a_5, h_5, m_5 and c_5 are material parameters. When the DRX volume fraction X_{DRX} is obtained, the grain size (d_{drex}) of new formed grains, which are generated by the process of DRX, can be calculated as

$$d_{drex} = a_8 d_0^{h_8} \varepsilon^{n_8} \dot{\varepsilon}^{m_8} \exp\left(Q_8/RT\right) + c_8 \tag{7}$$

where Q_8 is the activation energy for recrystallization, a_8, h_8, m_8, n_8 and c_8 are material parameters. Therefore, the average grain size of the remaining original grains and new formed grains by DRX can be calculated as

$$d = d_0\left(1 - X_{DRX}\right) + d_{drex} X_{DRX} \tag{8}$$

where d_0 is the initial average grain size of the grains.

2.3. Microstructure dependent JCM-ms plastic model

Normally, the microstructure evolution during the deformation process will affect the mechanical behaviors. Actually, the material parameters for JMAK models were normally obtained according to the mechanical tests for hot working at low strain-rate conditions (0.01–10s^{-1}) [24,42], since it is difficult to test the microstructure evolution during the high strain-rate (10^3–10^6 s^{-1}) deformation conditions.

It was well reported that for conventional polycrystalline materials with grain sizes ranging from several to hundreds of micrometers, the yield strength or hardness will increase with decreasing grain size [29], which is usually expressed by the Hall-Petch equation:

$$\sigma_y = a_0 + \frac{k}{\sqrt{d_0}} \tag{9}$$

Some investigations considered the influence of grain refinement on the work hardening behavior to characterize the uniaxial compressive flow stresses from quasi-static to high strain-rate conditions for nanocrystalline aluminum, iron and copper [29–31].

In this work, a new plastic constitutive (JCM-ms) model considering the microstructure, i.e., the effect of Hall-Petch relationship and the temperature dependent work hardening rate was developed as follows:

$$\overline{\sigma} = \left[A_0 + \frac{k}{\sqrt{d}} + B\left(\frac{T_0 - \frac{T}{2}}{T_0}\right)^{n_2} (\varepsilon)^n\right]\left[1 + C\ln\left(\frac{\dot{\varepsilon}}{\dot{\varepsilon}_0}\right)\right]\left[1 - \left(\frac{T - T_r}{T_m - T_r}\right)^m\right] \tag{10}$$

where the parameters of the JCM-ms model as well as the parameters to determine the grain size are listed in Table 3. The parameters A_0 and k were calibrated according to the measured principal and thrust forces at different uncut chip thickness values.

2.4. Energy-density based ductile failure model

2.4.1. Ductile damage initial law

The complete material deformation process for ductile metals includes the elastic and plastic regimes, along with stable work hardening and damage (or failure) stages, as shown in Fig. 1. In metal cutting processes, large-scale plastic deformation occurs along the ASB, and are involved in material removal during chip formation. As shown by Chen et al. [14], the evolution law of damage, or the failure stage can characterize the flow softening behavior of the flow stresses.

In this work, the JC damage initial law and an energy density based ductile failure law were applied to characterize the flow stress at the damage stage.

The ductile damage stage initiates when the cumulative equivalent plastic strain reaches the failure initial strain ε_{oi} which is defined by JC damage law [43] as

$$\varepsilon_{oi} = \left[d_1 + d_2 \exp\left(d_3\eta\right)\right]\left[1 + d_4 \ln\left(\frac{\dot{\bar{\varepsilon}}^{pl}}{\dot{\varepsilon}_0}\right)\right]\left[1 + d_5\left(\frac{T - T_r}{T_m - T_r}\right)\right] \tag{11}$$

where $d_1 \sim d_3$ are material constants related to the stress state, d_4 and d_5 are constants related to loading strain-rate and temperature. These parameters are normally obtained by mechanical experiments with notched and axisymmetric specimens at different strain-rates and temperatures. In this work, the parameters for *Ti-6Al-4V* alloy are listed in Table 4. η is the stress triaxiality that can be defined by the dimensionless hydrostatic pressure [44] as

$$\eta = \frac{-p}{q} = \frac{\sigma_m}{\overline{\sigma}} \tag{12}$$

where p is the pressure stress, q and $\overline{\sigma}$ represent the von Mises equivalent stress; σ_m is the average of three normal stresses, which can be defined as

Table 3
Parameters of the material model for *Ti-6Al-4V* alloy.

Parameters of the material constitutive models									
JCM-ms model	A_0/MPa	k	B/MPa	n	C	m	n_2	T_0/°C	
	300	1295.3	911.446	0.306	0.012	0.952	0.349	462.314	
DRX parameters [21,23,24]	a_1	a_2	h_1	m_1	c_1	R (J·mol^{-1} K^{-1})	Q_1	β_d	k_d
	0.0064	0.8	0	0.0801	0	8.3145	30,579	0.9339	0.5994
	a_5	h_5	m_5	c_5	Q_5				
	0.022	0	0.11146	0	26,430				
	a_8	h_8	m_8	n_8	c_8	Q_8	a_{10}		
	1120	0	−0.088	0	0	−36,848	0.0311		

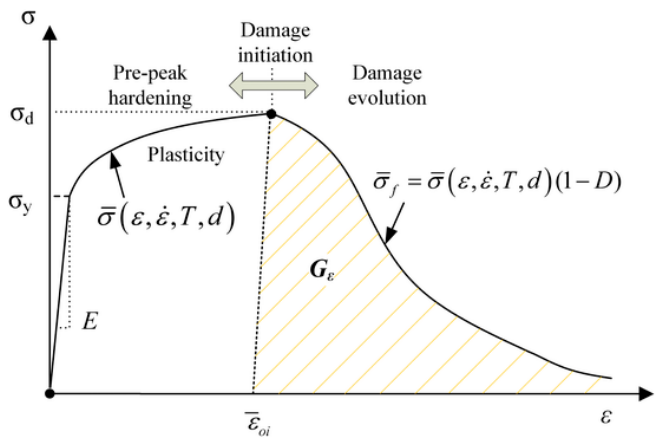

Fig. 1. The schematic of the flow stress evolution for ductile metals.

Table 4
Ductile failure parameters of *Ti-6Al-4V* alloy [45].

d_1	d_2	d_3	d_4	d_5
−0.09	0.25	−0.5	0.014	3.87

$$p = -\sigma_m = -\frac{1}{3}\mathrm{tr}([\sigma]) = -\frac{1}{3}(\sigma_1+\sigma_2+\sigma_3) \tag{13}$$

$$q = \bar{\sigma} = \sqrt{\frac{3}{2}[S]:[S]} = \sqrt{\frac{1}{2}\left[(\sigma_1-\sigma_2)^2+(\sigma_2-\sigma_3)^2+(\sigma_3-\sigma_1)^2\right]} \tag{14}$$

2.4.2. Energy-density based damage evolution stage

When the deformation reaches the damage evolution stage, the flow stress will decrease with increasing strain, as shown in Fig. 1. In this work, an energy density-based method which was first developed in the FE simulation of *Ti-6Al-4V* alloy for high speed cutting process was applied to characterize the flow stress at the damage evolution stage [46]. The energy density-based method can maintain the flow stress throughout the damage evolution stage which is helpful to reduce the mesh dependence in cutting simulation [13,47].

The flow stress at the damage evolution stage is defined based on a damage parameter D as:

$$\bar{\sigma}_f = \bar{\sigma}(\varepsilon,\dot{\varepsilon},T,d)(1-D) \tag{15}$$

where D is the stiffness degradation coefficient which can be determined in terms of the evolution of energy density G_ε as:

$$D = \frac{1-\exp\left(-a\int_0^{\varepsilon_f}\frac{\bar{\sigma}_y}{G_\varepsilon}d\bar{\varepsilon}\right)}{1-\exp(-a)} \tag{16}$$

where a is a softening coefficient, in this work, $a = 1$. The failure energy density G_ε is defined as

$$G_\varepsilon = \frac{G_f}{L} = \int_{\bar{\varepsilon}_{oi}}^{\bar{\varepsilon}_f^{pl}}\sigma_y d\bar{\varepsilon}^{pl} \tag{17}$$

where G_f is the failure energy, L is the characteristic length of the element which depends on element geometry. In this work, the stiffness degradation coefficient was set as $D = 1$ when the failure energy density reaches 0.99 given value.

2.5. Modeling procedure of the plastic, damage and microstructure constitutive model

The developed material model including the plastic model considering grain refinement, as well as the coupled damage model and microstructure prediction model, were programmed by a user-subroutine. The modeling procedure is illustrated in Fig. 2.

At the initial step of the procedure, stress is updated following the Hooke's elastic law. The stress tensors are defined as [13]:

$$\sigma_{ij}^{k+1} = \sigma_{ij}^{k} + \lambda tr(\varepsilon^e)\mathbf{I} + 2\mu\Delta\varepsilon^e \tag{18}$$

where $\sigma_{ij}{}^k$, $\sigma_{ij}{}^{k+1}$ are the stress tensors at the increment of k and $k+1$, respectively; λ and μ are the first and second order of Lame's constants; $\boldsymbol{I}$ is the identity matrix; $tr(\varepsilon^e)$ is the trace of stress tensor.

The von Mises stress is updated based on the elastic-plastic theory [48]and calculated by

$$\sigma_m^{k+1} = \bar{\sigma}_y^{k+1} + 3G\Delta\varepsilon^k \tag{19}$$

where G and $\Delta\varepsilon^k$ are the shear modulus and the increment of equivalent plastic strain, respectively. The yield stress is calculated by

$$\bar{\sigma}_y^{k+1} = \bar{\sigma}_y^{k} + H^k\Delta\varepsilon^k \tag{20}$$

where H^k represents the slope of the hardening curve, i.e., the stress-strain curve defined by Eq. (10) .

$$H^k = \frac{d\sigma_y}{d\bar{\varepsilon}} \tag{21}$$

The increment of the equivalent plastic strain can be determined by

$$\Delta\varepsilon^k = \frac{\sigma_m^{k+1}-\bar{\sigma}_y^{k}}{3G+H^k} \tag{22}$$

Therefore, the equivalent plastic strain is updated by

$$\varepsilon^{k+1} = \varepsilon^k + \Delta\varepsilon^k \tag{23}$$

afterwards, the yield stress is updated by Eq. (20). The deviatoric stress tensor can be updated to keep the stress return to the von Mises yield surface by a factor of radial returning algorithm m_r.

$$\mathbf{s}_{ij}^{k+1} = \boldsymbol{\sigma}_{ij}^{k+1}m_r + \sigma_{mean} \tag{24}$$

$$m_r = \frac{\bar{\sigma}_y^{k+1}}{\sigma_m^{k+1}} = \frac{\bar{\sigma}_y^{k+1}}{\bar{\sigma}_y^{k+1}+3G\Delta\varepsilon^k} \tag{25}$$

At damage evolution stage, failure initial strain is calculated by Eq. (11). If $\varepsilon^{k+1} \geq \varepsilon_{oi}$, flow stress will decrease with the increasing strain. Deviatoric stress and von Mises stress are updated by the stiffness degradation factor as follows

$$\begin{cases} S_{ij}^d = S_{ij}^p\left(1-D^{k+1}\right) \\ \sigma_{mises}^d = \sigma_{mises}^p\left(1-D^{k+1}\right) \end{cases} \tag{26}$$

where $S_{ij}{}^p$, $S_{ij}{}^d$are the Deviatoric stresses at plastic and damage stages, respectively. $\sigma_{mises}{}^p$, $\sigma_{mises}{}^d$ are the von Mises stresses at plastic and damage stages, respectively. D^{k+1} is the stiffness degradation coefficient at increment of $k+1$, and it can be calculated using Eq. (16).

After the stress updates, the grain size and micro-hardness will be updated according to the schematic procedure shown in Fig. 3 and calculated by equations Eqs. (4)–(9). Additionally, the updated grain size will be used to calculate the yield stress.

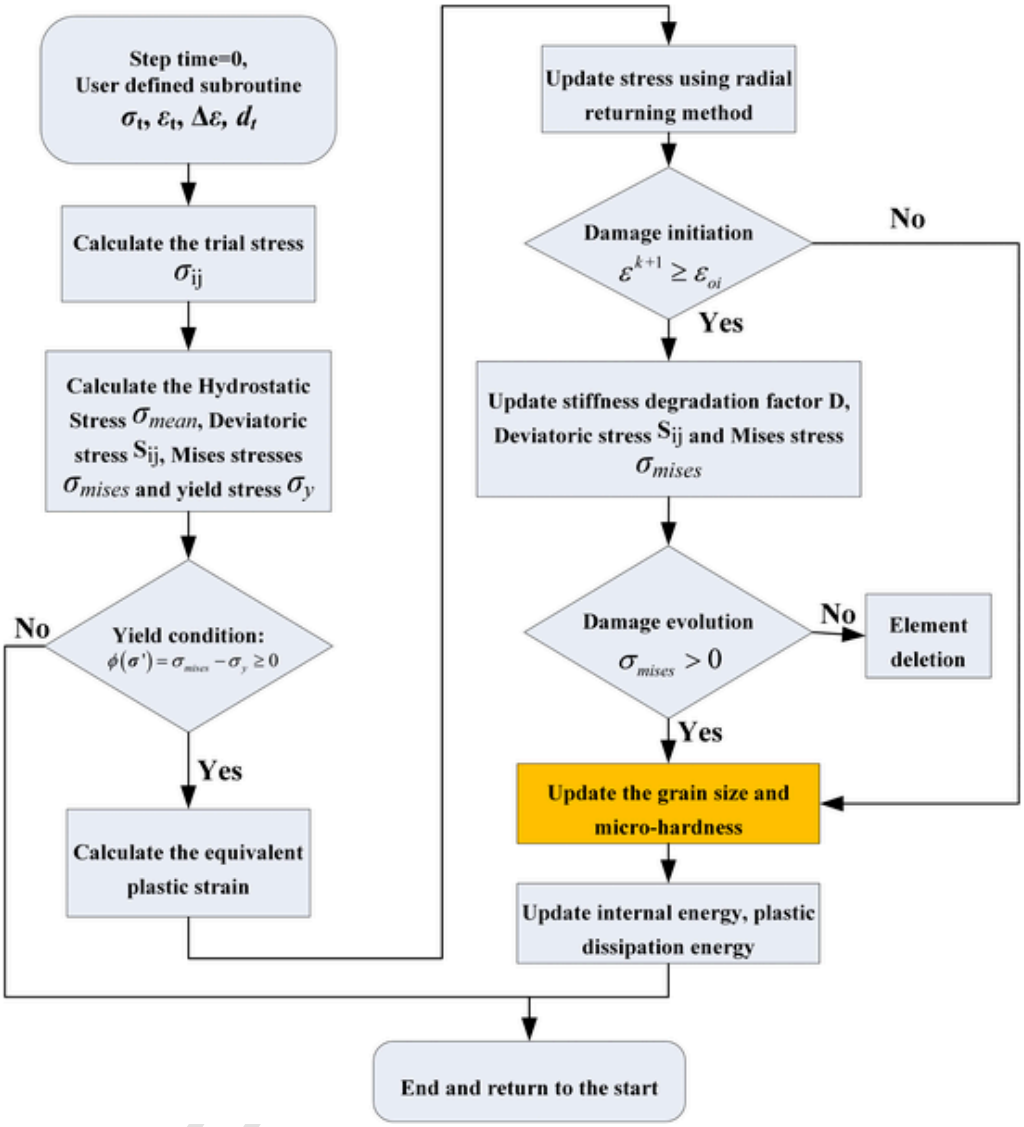

Fig. 2. The flow chart of the subroutine for the constitutive modeling.

3. Orthogonal cutting experiment and numerical modeling

3.1. Experimental details

To validate the accuracy of the developed material model and the cutting simulation approach, orthogonal cutting tests for *Ti-6Al-4V* alloy with different cutting-edge radii and uncut chip thickness values were proposed under dry conditions. The cutting tests were carried out on a HAAS™ TL-2 CNC lathe using uncoated carbide tool inserts type TPG432 k313 (provided by Kennametal® Inc.) with a rake angle of 0° and a flank angle of 11°. During the tests, the principal and thrust forces were measured by a dynamometer (type: Kistler® 9121) and a data acquisition system with a sampling rate of 3.33 kHz. Each cutting condition was repeated three times with new cutting edge to reduce the influence of random errors. The thickness of the disk workpiece is 3.175 mm. The experimental setup and conditions are shown in Fig. 4 and Table 5, respectively.

3.2. Finite element model for cutting simulation

The finite element simulation model of the orthogonal cutting process was developed using the ABAQUS/Explicit™ software. The schematic of the FE model is shown in Fig. 5. The size of the workpiece is 0.8 mm × 0.5 mm. The workpiece is meshed with the type of CPE4RT elements, and the mesh numbers of the workpiece and tool are 22,400 and 330, respectively. The rake and clearance angles were identical to that employed during experimentation. A Coulomb friction model, with a constant coefficient of friction 0.24, is applied to the tool-work contact surface and is set for tool-work interface. The developed microstructure related plastic behavior and the energy density-based ductile failure parameters were applied to the entire workpiece. The failure energy G_f and the failure energy density G_e for the chip formation are 10 ($\times 10^3$ J/m^2) and 3.912 ($\times 10^9$ J/m^3), respectively. Additionally, to avoid the mesh distortion due to severe deformation, an additional displacement criterion was applied to workpiece. In the FE model, the minimum length of the elements in workpiece surface is approximately 1.06 μm. In this work, the element will be deleted when the accumulated displacement reaches 19 μm to avoid mesh distortion.

4. Results and discussion

4.1. Validation of the simulation results

4.1.1. Forces

To validate the developed material model, the simulated principal and thrust forces at different edge radii (<5, 28 and 50 μm) and uncut

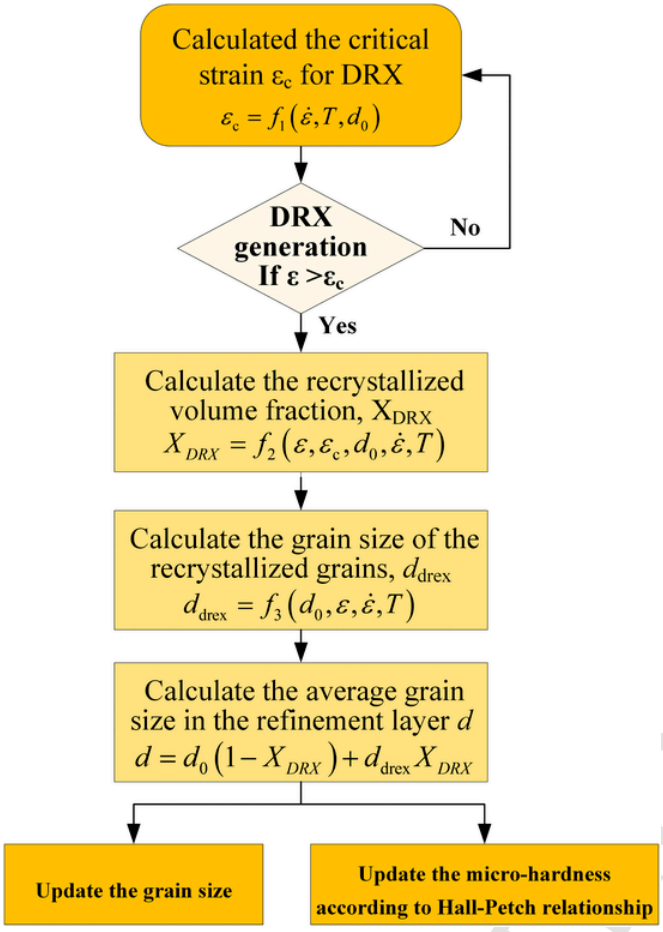

Fig. 3. The flow chart of the subroutine for microstructure model.

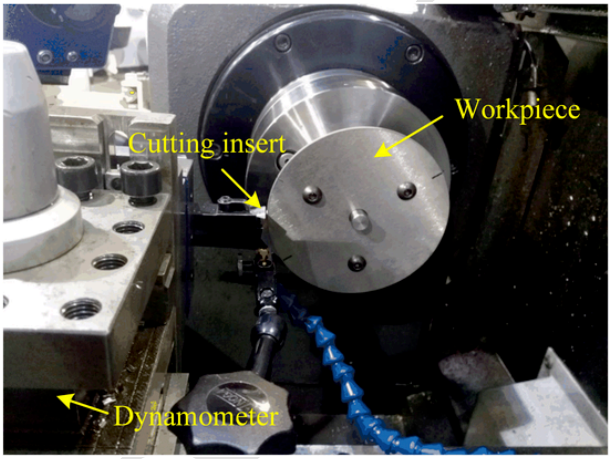

Fig. 4. Experimental setup for orthogonal cutting of *Ti-6Al-4V* alloy.

Table 5
Experimental conditions for the orthogonal cutting of *Ti-6Al-4V* alloy.

	Edge radius (μm)	Uncut chip thickness (μm)	Cutting speed (m/min)
Set 1	<5, 28 and 50	60	100
Set 2	50	20, 30, 40, 50 and 60	100

chip thickness values (20-60 μm) were compared with the measured forces. In this work, two sets of simulation results were carried out to compare the principal and thrust forces. One set was simulated by the temperature dependent JCM model, the other set was proposed by the developed JCM-ms material model considering microstructure evolution. The comparison of the forces at different edge radii are shown in Fig. 6. The experimental forces at different edge radii were identical with the previous work with dry cutting condition [49].

Although some parameters of the plastic model and ductile damage model for JCM and JCM-ms model are identical, the predicted forces by the JCM model are lower than those with JCM-ms model. The relative errors of the principal forces between the results by JCM and experiments are 2.2 %–6.4 %, while, the relative errors of the principal forces between the results by JCM-ms and experiments are 0.4 %–5.8 %. As indicated in Fig. 6b, the edge radius has a greater influence on the thrust forces. The variation of edge radius will affect material flow ahead of the cutting edges. That is, it will affect the ratio of the material being ploughed to the machined surface due to the different edge radii. The relative errors of the measured thrust forces and the predicted results by JCM-ms model are between 2.6 %–9.1 %, which are much less than the relative errors between the measured and simulated thrust forces by JCM model (10.2 %–21.7 %). That is, the layer of grain refinement at the top machined surface layer will lead to an increase in the work hardening rate according to the proposed JCM-ms model. As shown in the compared thrust forces, the effect of the grain refinement work hardening is enhanced with the increasing edge radius, from ~5 to 50 μm.

To further validate the accuracy of the predicted forces, the measured and predicted principal and thrust forces by JCM-ms model are compared at different uncut chip thicknesses, as shown in Fig. 7. Both the predicted principal and thrust forces agreed well with the measured forces. The relative errors between the measured and simulated principal forces varied from 0.7 % to 12 %, while, the relative errors between the predicted and measured thrust forces are approximately 2.3 %–9.1 %. Additionally, the principal force increases almost linearly with the increasing uncut chip thickness, however, the variation of the thrust force is smaller than that of the principal force. At the same uncut chip thickness, with larger edge radius more material ahead of cutting edge will be compressed on the machined surface due to the ploughing effects [49]. Therefore, the edge radius has greater influence on the thrust forces than the uncut chip thickness. Overall, the largest relative error between the simulated and measured forces is 12 %. Therefore, both the simulated principal and thrust forces predicted by the proposed material model agree well with the measured experimental results for most conditions.

4.1.2. Chip morphology

Chip morphology is an important characteristic which reflects the material deformation at high strain-rate, strain and complex thermal loading conditions. It was reported that ultra-fine grains can be generated during high-speed (600 m/min) machining of *Ti-6Al-4V* alloy due to the rotation dynamic recrystallization [29]. In this work, the microstructures of the cross-section of the segmented chips and workpiece normal to the cutting speed direction was analyzed. The experimental and numerically predicted chip morphology, along with the grain size distribution are shown in Fig. 8. Additionally, the measured and simulated chip morphologies, including the peak, valley and pitch (as indicated in Fig. 8f) of the segmented chips at the conditions of different edge radii and uncut chip thicknesses are compared with each other, as listed in Table 6. Note that, the largest relative errors between the simulated and experimental peak and valley values are <7.8 % and 12.3 %, respectively. The relative errors for the pitch results are <24.1 %. Overall, the predicted segmented chips agreed well with the measured chip morphologies. The high predictive accuracy of the segmented chip morphologies indicates that the ductile damage behavior of the material along the ASB at the stage of damage evolution was properly implemented, as is described in Fig. 1.

Additionally, grain refinement phenomena were mainly observed in three areas: i) along the ASB, ii) the chip root which contacts the tool

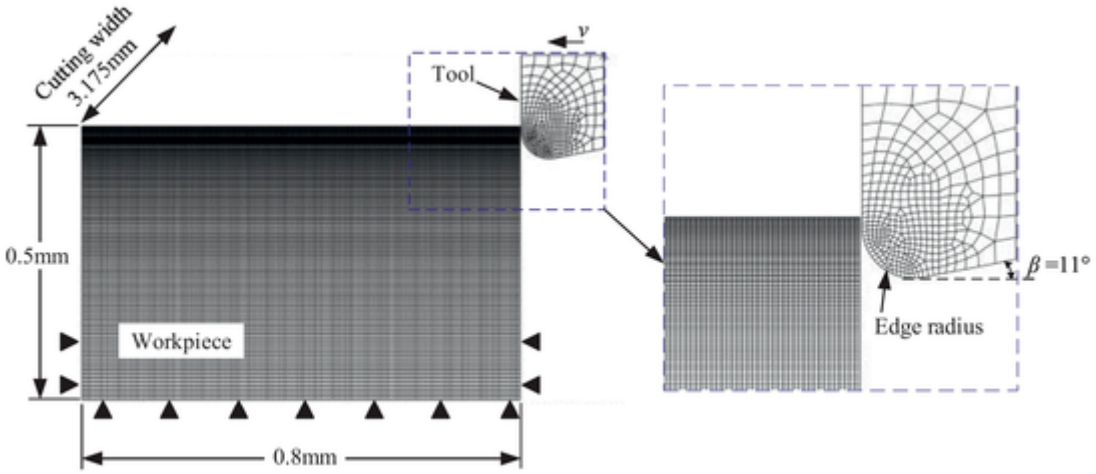

Fig. 5. The schematic of the FE simulation model of the orthogonal cutting process with cutting edge radius of 50 μm.

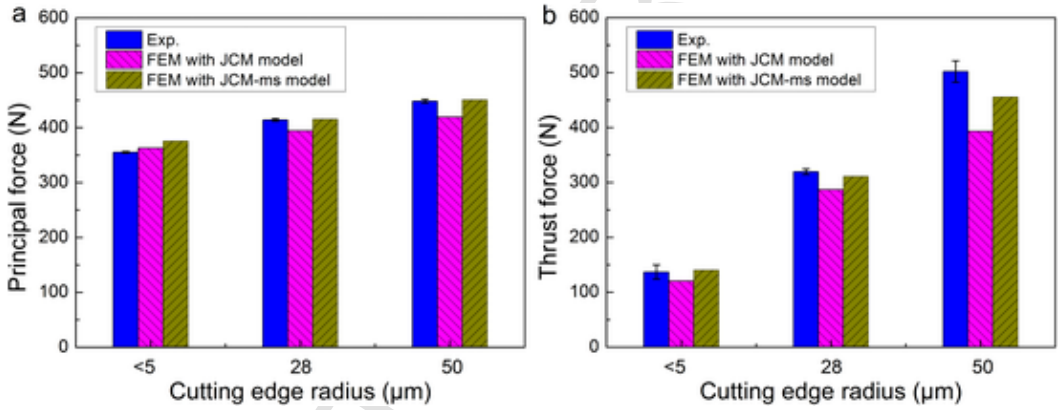

Fig. 6. Comparison of the measured and simulated (a) principal and (b) thrust forces with different cutting-edge radii.

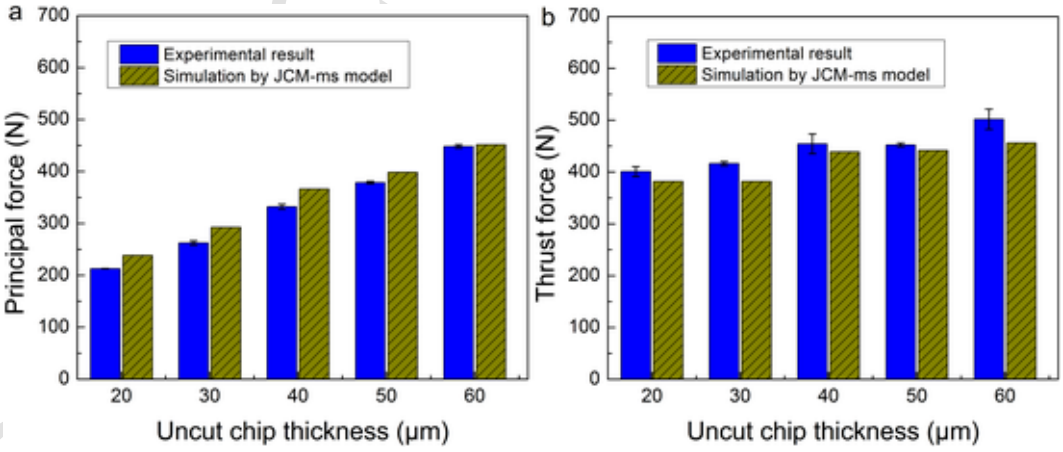

Fig. 7. Comparison of the measured and simulated (a) principal and (b) thrust forces at varying uncut chip thickness values

rake surface and iii) the machined workpiece surface. According to the Hall-Petch relationship, grain refinement will increase the mechanical strength and work hardening of the workpiece.

4.1.3. Microstructure at machined surface/subsurface

To further validate the distribution of grain size and the grain refinement behavior, microstructure of the cross-section of the machined samples was compared with the simulated grain size distribution of the machined surfaces at different edge radii and uncut chip thickness values, as shown in Fig. 9. With same length scale, the simulated grain size can be compared with the experimental results. As two (α and β) phases exist at the cross-section of the machined workpiece samples, the grain refinement phenomenon can be identified by the distribution of the β phases, especially for the thickness of the grain refinement layer near the machined surface. As shown in Fig. 9a-c, the thickness of the grain refinement layer increases with the increasing edge radius. There is no obvious grain refinement layer at the smallest edge radius (<5 μm), while, the thickness values of the grain refinement layers with the edge radii of 28 and 50 μm are 2.86 and 4.38 μm, respectively. Note that the simulated grain size at the machined surface layer with an edge radius

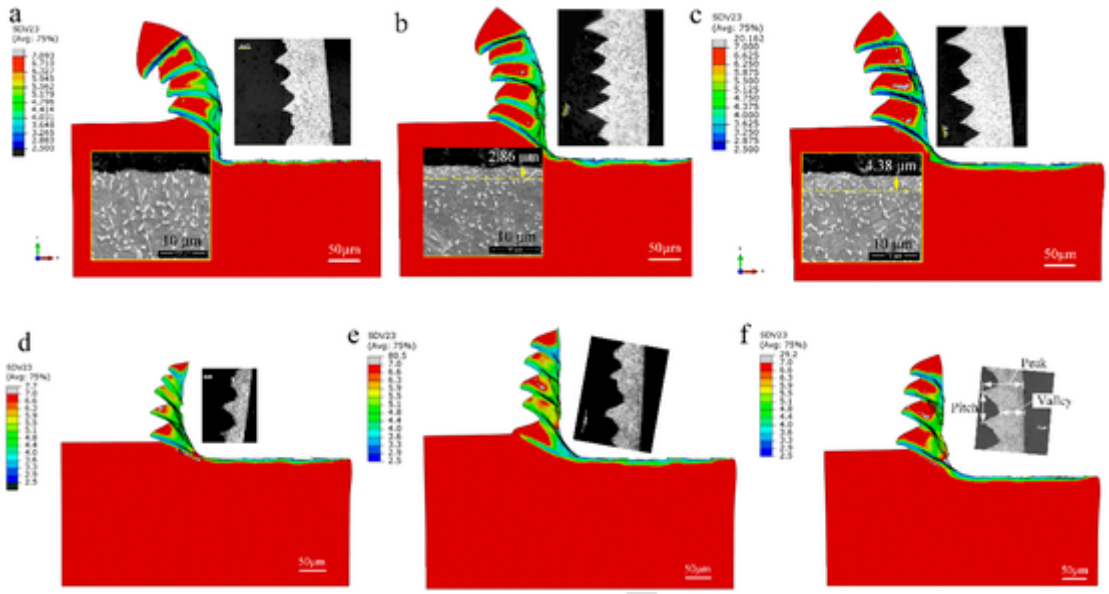

Fig. 8. Comparison of the predicted and measured chip morphology at different edge radii of (a) <5 μm (b) 28 μm (c) 50 μm; and at different uncut chip thickness values of (d) 30 μm (e) 40 μm and (f) 50 μm.

Table 6
Comparison of the simulated and experimental chip morphology.

Condition		Peak (μm)	Valley (μm)	Pitch (μm)
Edge radius <5 (μm)	Sim.	85.63	64.55	25.36
	Exp.	79.43	57.46	33.43
	Error	−7.8 %	−12.3 %	24.1 %
Edge radius 28 (μm)	Sim.	83.64	63.75	28.74
	Exp.	87.99	60.82	33.29
	Error	4.9 %	−4.8 %	13.7 %
Edge radius 50 (μm)	Sim.	86.15	55.66	40.14
	Exp.	89.16	62.43	45.96
	Error	3.4 %	10.8 %	12.75
Uncut chip thickness 30 (μm)	Sim.	56.56	24.55	43.42
	Exp.	57.62	25.54	56.28
	Error	1.8 %	3.9 %	22.8 %
uncut chip thickness 40 (μm)	Sim.	74.04	42.94	41.90
	Exp.	75.72	45.29	49.07
	Error	2.2 %	5.2 %	14.6 %
uncut chip thickness 50 (μm)	Sim.	85.74	45.86	55.25
	Exp.	83.79	49.44	56.28
	Error	−2.3 %	7.3 %	1.8 %

of 50 μm is approximately 2.5 μm, and the grain size of the workpiece is about 7 μm. Additionally, the thickness values of the grain refinement layers at the uncut chip thicknesses of 30 and 50 μm with identical edge radius are close to each other (Fig. 9d and e). Therefore, the grain refinement is more pronounced with larger edge radii, and grain refinement layers will increase the flow stresses during the cutting process, which consequently will lead to higher thrust forces compared with the model without grain size dependent work hardening rate, as indicated in Fig. 6b. Overall, for the conditions with different edge radii and uncut chip thickness values, the simulated grain refinement agree well with the experimental microstructure at the cross-section of the machined surface.

4.2. Effect of cutting edge on material flow ahead of the cutting edge

The grain refinement behavior in the machined surface is related to the material flow ahead of the cutting edge. Normally, there is a stagnation point ahead of the rounded cutting edge, where the material ahead of the stagnation point will form the chip and material beneath the stagnation point will be compressed/ploughed into the machined surface. It is difficult to obtain the position of stagnation points by experimental methods. For numerical methods, the stagnation point cannot be obtained by modeling methods with a predefined sacrificial (or separation) layer between the uncut chip layer and the workpiece. In this work, the stagnation point is characterized by the material displacement normal to the machined surface, as shown in Fig. 10. Material flows downward to the machined surface, as is shown by the denoted arrows. Therefore, the stagnation point can be identified by the highest location of the arrows at the workpiece which contacts with the cutting edge, as shown in Fig. 10c. The distances from the stagnation point S to the machined workpiece surface at different conditions were measured and shown in Fig. 10h and i. Note that the height of the stagnation point increase greatly from almost zero to 18.2 μm with the increasing edge radius from <5 μm to 50 μm. The increased height of the stagnation point, indicates that more material inside of the uncut chip thickness will be compressed on the machined surface. That is identical with the phenomena of the grain refinement and the increase of thrust forces with the increasing edge radius. While, for different uncut chip thickness values, the height of the stagnation point increases slightly from 20 to 50 μm uncut chip thickness, as shown in Fig. 10e-h. It is also consistent with the increasing thrust forces at different uncut chip thickness values. Note that the stagnation point may vary periodically during the formation of ASB's.

Additionally, the variation of the stagnation point not only affects the grain refinement at the machined surface layer, but it can also influence the surface roughness along the cutting direction. The simulated surface displacement along the normal direction (normal to the machined surface), as well as the measured surface topography, were analyzed using a non-contact ZYGO™ scanning white light interferometer are shown in Fig. 11. The scale of tested area is 110 μm × 110 μm. With an edge radius of 5 μm, there is no obvious displacement along the normal direction both in either the simulated or experimentally measured surface topography, since most material in the uncut chip thickness was moved forward to form the chips, as indicated in Fig. 10a. As shown in Fig. 11b and c, the simulated machined surface generated periodical fluctuation along the speed direction. In this work, the adjacent distance of the peak or valley at the machined surface which is caused by the variation of the stagnation position during the formation of the ASB is calculated. The fluctuation distances of the simulated results in Fig. 11b and c are very close to the measured surface topography in Fig. 11b' and c'. That is, the periodical fluctuation with larger edge radius is

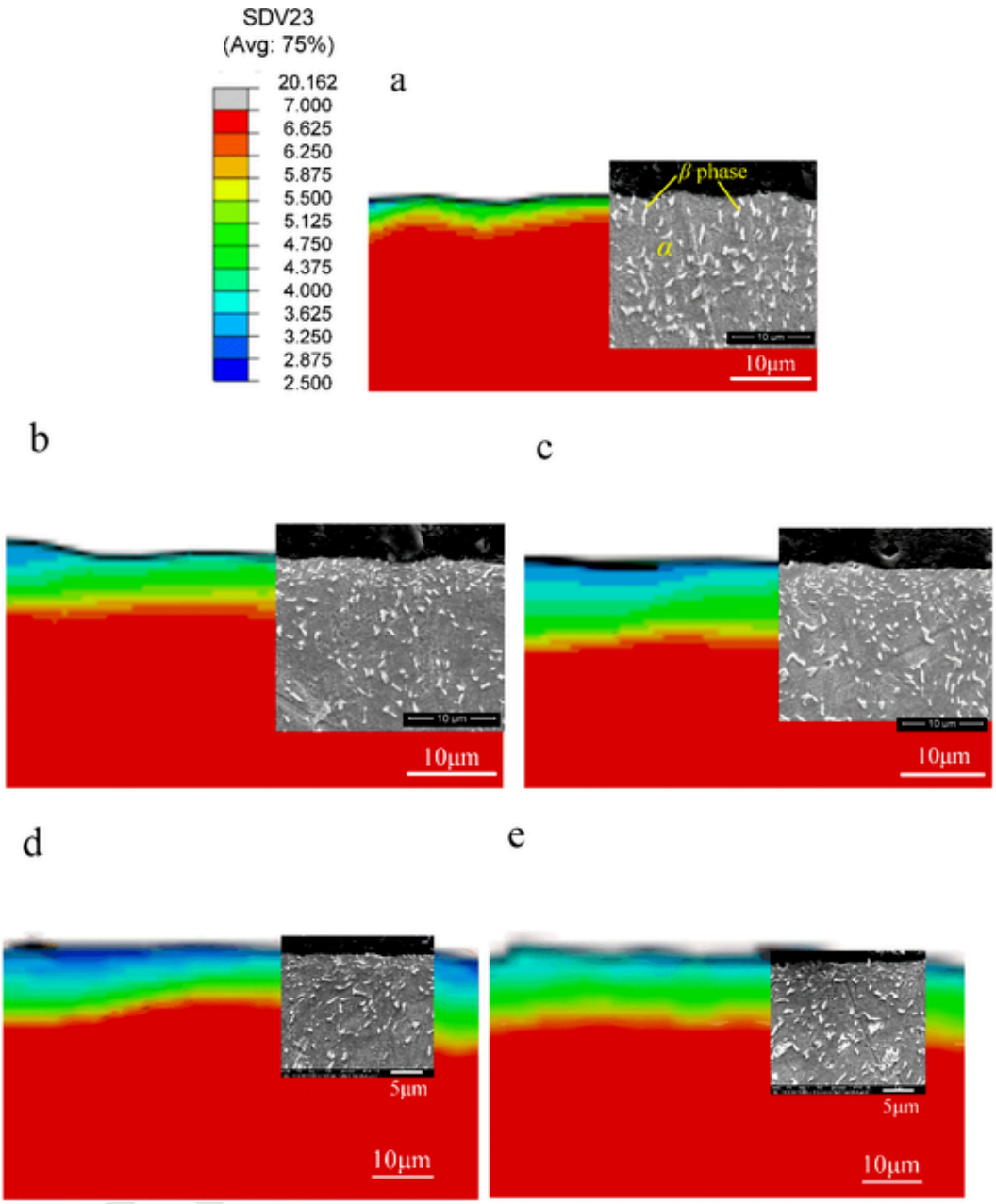

Fig. 9. Comparison of the predicted grain size distribution and machined subsurface microstructure at different edge radii of (a) < 5 μm (b) 28 μm and (c) 50 μm and at uncut chip thickness of (d) 30 μm and (e)50 μm.

related to the variation of the stagnation points during the formation of the ASB.

4.3. Simulated surface integrity

4.3.1. Micro-hardness

Normally, the increase in micro-hardness observed in the machined surface/subsurface is related to the material strengthening caused by the thermo-mechanical plastic deformation. Furthermore, the mechanical behavior is strongly dependent on the flow stress at different loading strains, strain-rates and temperatures. Microstructurally, micro-hardness evolution is dependent on the deformation-induced twinning, dislocation accumulation, as well as the grain size evolution [50]. As reported by Hughes and Korellis [51], subsurface deformation which is caused by large sliding or rubbing loads strongly contributes to the increase in subsurface hardness in cutting or metal working. In this work, the measured subsurface hardness and the simulated plastic deformation along the cutting direction were analyzed, comparatively. The subsurface micro-hardness was measured by a SUN-TEC™ Tester with a Vickers indenter at loading force of 100 mN and dwell time of 10 s. The measured micro-hardness at different edge radii (Fig. 12a) is identical with results presented in the previous work [49]. Although the micro-hardness of the subsurface by the sharp (about 5 μm edge radius) tool is slightly higher than other conditions, the decreasing gradient with increasing depth from machined surface at the largest edge radius (50 μm) is higher than the results with smaller edge radii.

The simulated displacement along the direction of cutting speed with different edge radii are shown in Fig. 12b. It is noted that the displacement decreasing gradient of the fitted curves with different edge radii are very similar with the hardness results. The displacement along the cutting direction is caused by the shear deformation generated by the tool-workpiece contact during cutting. The surface displacement with the sharp tool is about 6 μm, which is lower than that the 9.6 and

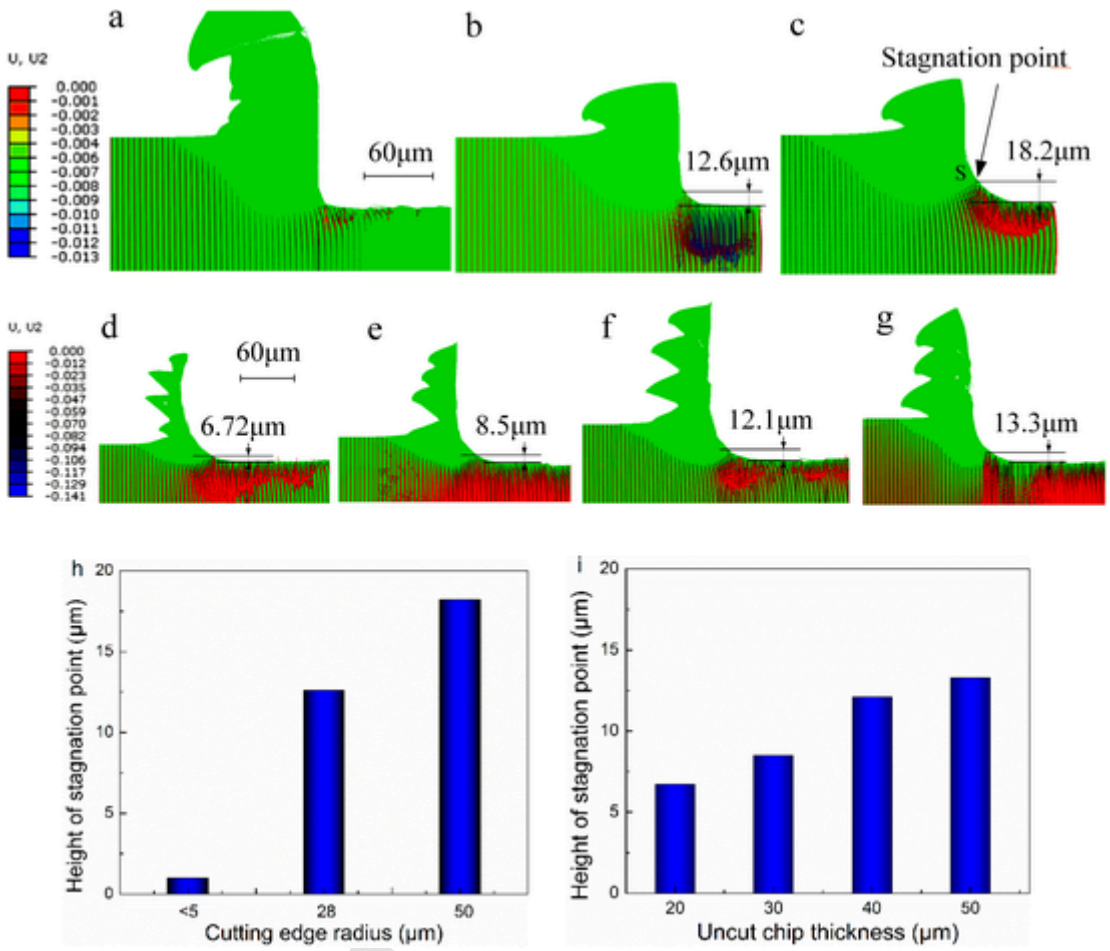

Fig. 10. The stagnation positions at different edge radii of (a) < 5 μm (b) 28 μm and (c) 50 μm and at uncut chip thicknesses of (d) 20 μm (e) 30 μm (f) 40 μm and (g) 50 μm (h) the height of stagnation point at different edge radii and (i) uncut chip thicknesses.

13.8 μm induced by the edge radii of 28 and 50 μm, respectively. Additionally, the thickness of the shear deformation is about 20 μm which is smaller than that produced with larger edge radii tools. As seen in Figs. 8 and 9, there is no obvious grain refinement at the condition with sharp edge. While, the thickness values of grain refinement layers are 2.86 and 4.38 μm for the edge radii of 28 and 50 μm, respectively. Therefore, the degree of the subsurface shear deformation is highly related to the micro-hardness, and the thickness of the subsurface shear deformation is increased at larger edge radius. As indicated in Fig. 12b, when the displacement exceeds a critical value (approximately 8 μm for different edge radii), grain refinement will be generated at the top machined surface. Larger shear displacement at the top surface will lead to thicker grain refinement layer.

To check the micro-hardness with different uncut chip thickness values, the micro-hardness and the shear displacement at the uncut chip thicknesses (radial feed rate) of 20 and 50 μm are shown in Fig. 13a and b, respectively. The variation in the trends of the fitted curves of the hardness and displacement are similar. The micro-hardness at uncut chip thickness of 50 μm is slightly higher than that at uncut chip thickness of 20 μm. This is identical with the displacement comparison result. Additionally, the top surface displacement at the two conditions are higher than 10 μm which can be considered as the critical value for the uncut chip thicknesses of 20 and 50 μm, and grain refinement layers are both observed at the machined top surface for 20 and 50 μm uncut chip thickness conditions.

4.3.2. *Residual stress*

To further study the machined surface integrity, the residual stresses of a path of nodes along the depth from the machined surface were analyzed, as shown in Fig. 14. The predicted residual stresses for different depths from the machined surface were compared with the measured results obtained using an edge radius of 28 μm, as shown in Fig. 14a. The simulated and measured residual stresses exhibit similar trends, with the measured residual stresses slightly more tensile (or less compressive) than the simulated results. Tensile stresses were generated at the top surface (< 25 μm), while compressive residual stresses were generated in the subsurface at the depth of 25–150 μm, approximately. The distribution of the residual stress is related to the thermo-mechanical deformation at the machined subsurface. It should be noted that both the hardness and residual stress are time-dependent parameters which means the state of these parameters are different at the in-situ (cutting stage) and ex-situ (when the workpiece is cooling to the environmental temperature) states [2]. Additionally, the material deformation of the nodes path along the direction normal to the machined surface is shown in Fig. 14b. It should be noted that the trend of the displacement normal to machined surface is similar to that of the residual stresses, except for the displacement of few points near the top surface, which may be caused by the element distortion.

To study the mechanism of the machined subsurface residual stresses, the predicted residual stresses and displacement normal to the machined surface with different edge radii and with different uncut chip thicknesses are shown in Figs. 15, and 16, respectively. Note that the edge radius and uncut chip thickness have similar influence on the variation of the residual stresses and the displacement normal to the

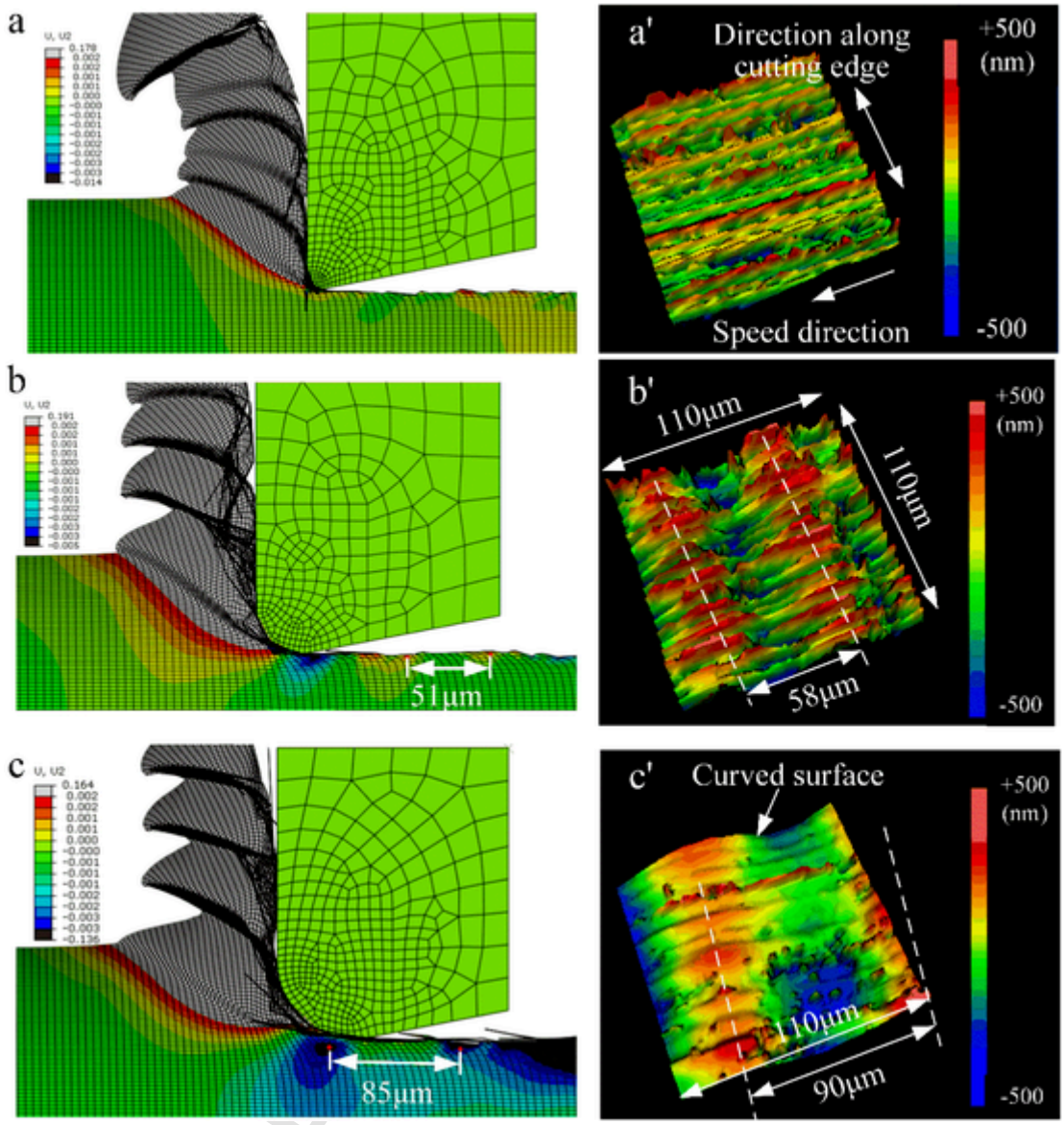

Fig. 11. Simulated displacement normal to the machined surface with edge radii of (a) < 5 μm (b) 28 μm (c) 50 μm and the measured surface morphology [49] at the edge radii of (a') < 5 μm (b') 28 μm (c') 50 μm.

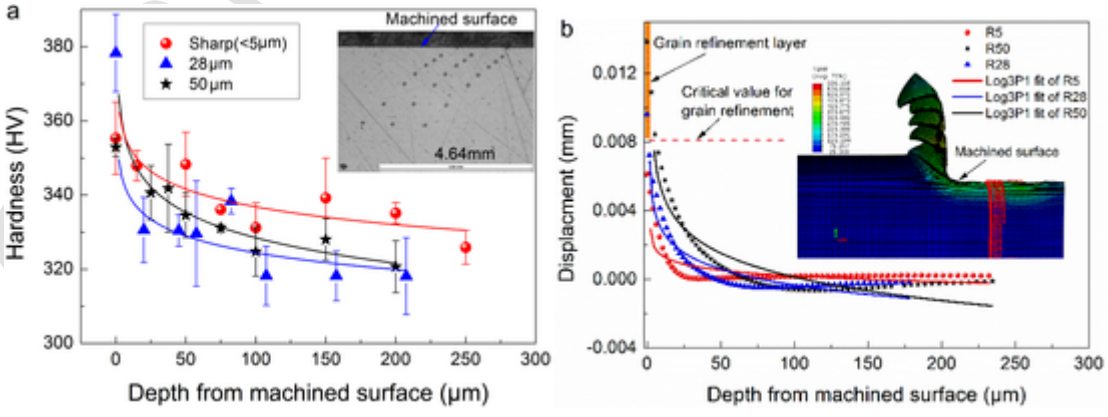

Fig. 12. Comparison of the (a) measured micro-hardness of the machined subsurface and (b) the displacement along the cutting direction at different cutting-edge radii conditions with uncut chip thickness of 60 μm.

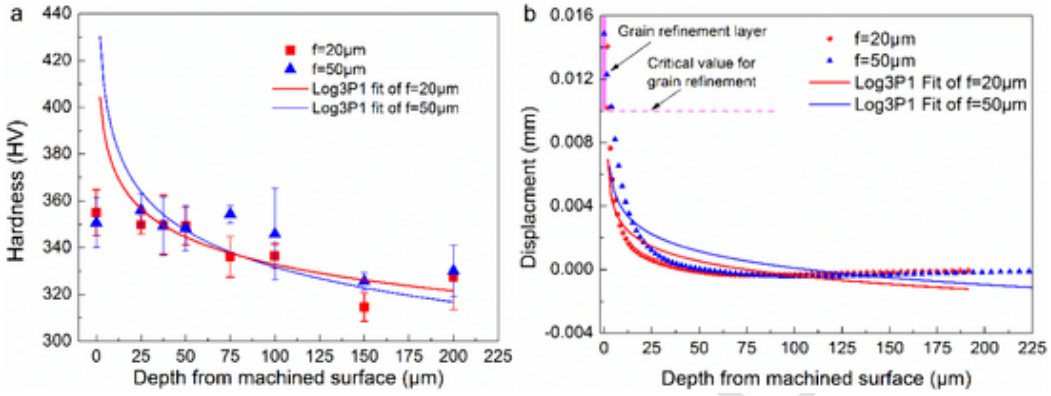

Fig. 13. Comparison of the (a) measured micro-hardness of the machined subsurface and (b) the displacement along the cutting direction at different uncut chip thickness values with edge radius of 50 μm.

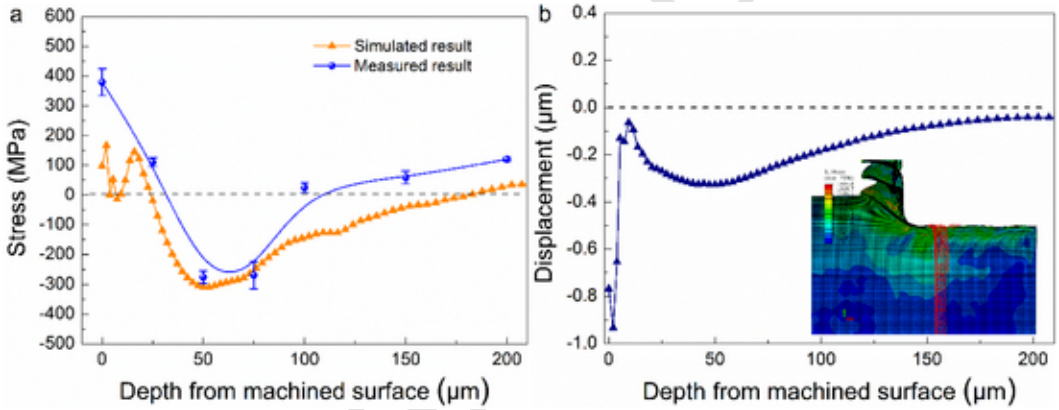

Fig. 14. Comparison of the (a) measured and simulated residual stress and (b) the displacement normal to machined surface at edge radius of 28 μm and uncut chip thickness of 60 μm.

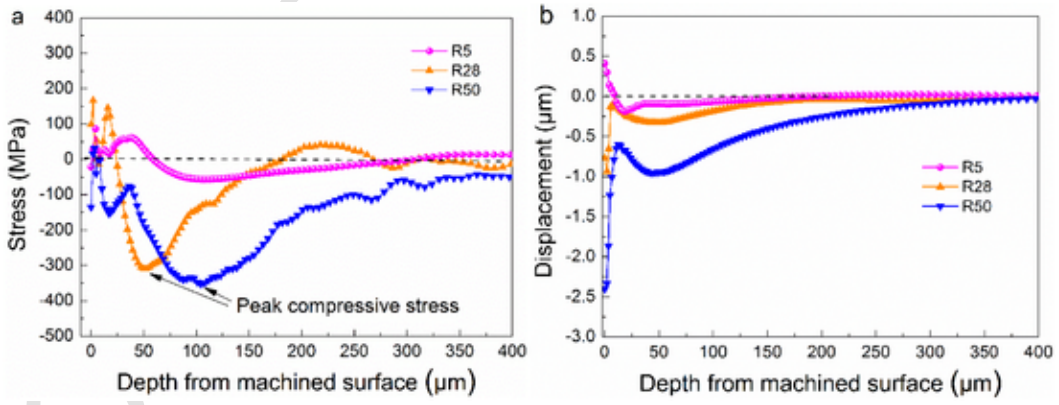

Fig. 15. Comparison of the simulated (a) residual stress and (b) the displacement normal to machined surface at different edge radii with uncut chip thickness of 60 μm.

machined surface, which further indicates the effect of the material being compressed to the machined surface on the subsurface residual stress field. The variation of the cutting edge significantly affects the material flow ahead of the cutting edge. As indicated in Fig. 10, the height of the stagnation point with edge radii of 28 and 50 μm are 12.6 and 18.2 μm, respectively, which is substantially higher than that observed with sharp cutting edge. Additionally, the peak compressive stresses are −309 MPa and -352 MPa at the edge radii of 28 and 50 μm, respectively, much higher than that (−56 MPa) with sharp cutting edge, while, the height of the stagnation points at the uncut chip thickness values of 20, 40 and 60 μm are 6.72, 12.1 and 18.2 μm, respectively. They are similar to the variation of the peak compressive stresses at different uncut chip thickness values. Therefore, as shown in Figs. 15a and 16a, the height of the stagnation point affects the ratio of the material which will be compressed to the machined surface, and it is approximately proportional to the peak compressive stresses for different conditions.

5. Conclusions

In this work, a finite element model employing a JCM-ms constitutive model was proposed to simulate the material removal and predict surface integrity in the orthogonal cutting of *Ti-6Al-4V* alloy. Grain refinement dependent work hardening was considered in the plastic

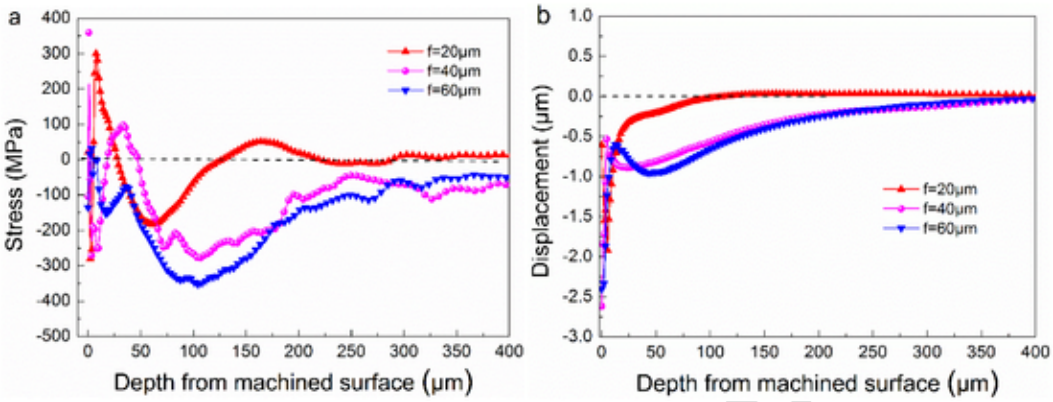

Fig. 16. Comparison of the simulated (a) residual stress and (b) the displacement normal to machined surface at different uncut chip thickness with edge radius of 50 μm.

model, while, an energy density-based failure behavior was applied to generate the chip formation and material removal ahead of the cutting edge. The simulation results were validated by the orthogonal cutting experiments of *Ti-6Al-4V* alloy with different edge radii and uncut chip thickness values. Surface integrity including the grain refinement, stagnation points, micro-hardness and residual stresses were analyzed according to the simulation results. The following conclusions can be draw from this work:

(1) DRX-based JMAK model was considered in the developed JCM-ms plastic model to characterize the grain refinement related work hardening rate. An energy density-based failure model was applied to the entire workpiece without a separation layer. The predicted principal and thrust forces agreed well with the measured results. For most conditions, the relative errors between the simulated and measured forces is <12 %. The grain size dependent work hardening behavior is helpful to improve the accuracy of the predicted thrust forces.
(2) Predicted chip morphology agreed well with those generated during experimentation. Grain refinement was most prominent along the ASB's and at the chip roots where the tool rake surface and the machined workpiece surface were in contact. The simulated grain refinement at the machined surface layer agreed well with the microstructure distribution at the cross-section of the machined subsurface. The thickness of grain refinement layer increased with increasing cutting-edge radius.
(3) The height of the stagnation point was measured by the simulation results. Larger heights of the stagnation points will lead to more material inside of the uncut chip layer being compressed on the machined surface, which in turn resulted in increased thrust forces, increased thickness of grain refinement layer, and changes in the micro-hardness and residual stress field distribution. The measured periodical fluctuation in surface morphology with larger edge radii is related to the variation of the stagnation points during the formation of the ASB.
(4) The degree of the subsurface shear deformation is highly related to the micro-hardness, and the thickness of the subsurface shear deformation increased with increasing edge radius. Larger shear displacement beyond the critical value at the top surface led to a thicker grain refinement layer. The residual stresses along the depth from machined surface is related to the displacement normal to the machined surface. The height of the stagnation point is approximately proportional to the peak compressive stresses for different conditions.
(5) The developed JCM-ms model and the energy density-based modeling method provide an accurate, high-fidelity prediction of the principal, thrust forces and subsurface grain refinement. This work also provided a greater understanding of the micro-hardness and residual stress field formation according to the material flow ahead of cutting edge, which will be helpful for the tool design and the investigation of surface integrity considering cutting-edge geometry.

Declaration of competing interest

The authors declare that they have no known competing financial interests or personal relationships that could have appeared to influence the work reported in this paper.

Acknowledgements

The authors would like to acknowledge the support from Mr. Adam Price who helped carrying out the orthogonal cutting tests at the Institute of Sustainable Manufacturing (ISM), University of Kentucky.

References

[1] Sagapuram D, Udupa A, Viswanathan K, Mann J.B, M'Saoubi R, Sugihara T, et al. On the cutting of metals: a mechanics viewpoint. J Manuf Sci E T ASME 2020;142 (11):1–46.
[2] Chen G, Ge J.Y, Lu L.P, Liu J, Ren C.Z. Mechanism of ultra-high-speed cutting of ti-6Al-4V alloy considering time-dependent microstructure and mechanical behaviors. Int J Adv Manuf Technol 2021;113:193–213.
[3] Arrazola P.J, Özel T, Umbrello D, Davies M, Jawahir I.S. Recent advances in modelling of metal machining processes. CIRP Ann 2013;62:695–718.
[4] Johnson G.R. A constitutive model and data for materials subjected to large strains, high strain rates, and high temperatures. In: Proc. 7th inf. sympo. ballistics, 541; 1983. p. 547.
[5] Khan A.S, Liang R. Behaviors of three BCC metal over a wide range of strain rates and temperatures: experiments and modeling. Int J Plast 1999;15:1089–109.
[6] Khan A.S, Huang S. Experimental and theoretical study of mechanical behavior of 1100 aluminum in the strain rate range 10–5–104s–1. Int J Plast 1992;8: 397–424.
[7] Yan S.L, Yang H, Li H.W, Yao X. Variation of strain rate sensitivity of an aluminum alloy in a wide strain rate range: mechanism analysis and modeling. J Alloys Compd 2016;688:776–86.
[8] Chen G, Lu L, Ren C, Ge X. Temperature dependent negative to positive strain rate sensitivity and compression behavior for 2024–T351 aluminum alloy. J Alloys Compd 2018;765:569–85.
[9] Wang J, Guo W, Gao X, Su J. The third-type of strain aging and the constitutive modeling of a Q235B steel over a wide range of temperatures and strain rates. Int J Plast 2015;65:85–107.
[10] Calamaz M, Coupard D, Girot F. A new material model for 2D numerical simulation of serrated chip formation when machining titanium alloy Ti–6Al–4V. Int J Mach Tool Manuf 2008;48:275–88.
[11] Sima M, Özel T. Modified material constitutive models for serrated chip formation simulations and experimental validation in machining of titanium alloy Ti–6Al–4V. Int J Mach Tool Manuf 2010;50:943–60.
[12] Chen G, Ren C, Qin X, Li J. Temperature dependent work hardening in Ti–6Al–4V alloy over large temperature and strain rate ranges: experiments and constitutive modeling. Mater Des 2015;83:598–610.
[13] Chen G, Ren C, Lu L, Ke Z, Qin X, Ge X. Determination of ductile damage behaviors of high strain rate compression deformation for ti-6Al-4V alloy using

experimental-numerical combined approach. Eng Fract Mech 2018;200:499–520.
[14] Chen G, Lu L, Ke Z, Qin X, Ren C. Influence of constitutive models on finite element simulation of chip formation in orthogonal cutting of ti-6Al-4V alloy. Procedia Manuf 2019;33:530–7.
[15] Zerilli F.J, Armstrong R.W. Dislocation-mechanics-based constitutive relations for material dynamics calculations. J Appl Phys 1987;61:1816–25.
[16] Mecking H, Kocks U.F. Kinetics of flow and strain-hardening. Acta Metall 1981; 29:1865–75.
[17] Wang Q, Shankar R.M, Liu Z, Cheng Y. Crystallographic texture evolutions of ti-6Al-4V chip foils in relation to strain path and high strain rate arising from large strain extrusion machining process. J Mater Process Technol 2022;305:117588.
[18] Khan A.S, Yu S, Liu H. Deformation induced anisotropic responses of Ti–6Al–4V alloy part II: a strain rate and temperature dependent anisotropic yield criterion. Int J Plast 2012;38:14–26.
[19] Liu H, Xu X, Zhang J, Liu Z, He Y, Zhao W, et al. The state-of-the-art on numerical simulation of the effect of microstructure and its evolution in metal cutting processes. Int J Mach Tool Manuf 2022;177:103890.
[20] Fanfoni M, Tomellini M. The Johnson-mehl-avrami-kohnogorov model: a brief review. Il Nuovo Cimento D 1998;20:1171–82.
[21] Wang Q.Q, Liu Z.Q, Wang B, Song Q.H, Wan Y. Evolutions of grain size and micro-hardness during chip formation and machined surface generation for ti-6Al-4V in high-speed machining. Int J Adv Manuf Technol 2016;82:1725–36.
[22] Sadeghifar M, Javidikia M, Songmene V, Jahazi M. Finite element simulation-based predictive regression modeling and optimum solution for grain size in machining of Ti6Al4V alloy: influence of tool geometry and cutting conditions. Simul Model Pract Theory 2020;104:102141.
[23] Xu X, Zhang J, Outeiro J, Xu B, Zhao W. Multiscale simulation of grain refinement induced by dynamic recrystallization of Ti6Al4V alloy during high speed machining. J Mater Process Technol 2020;286:116834.
[24] Quan G.Z, Luo G.C, Liang J.T, Wu D.S, Mao A, Liu Q. Modelling for the dynamic recrystallization evolution of ti-6Al-4V alloy in two-phase temperature range and a wide strain rate range. Comp Mater Sci 2015;97:136–47.
[25] Pan Z.P, Liang S.Y, Garmestani H, Shih D.S. Prediction of machining-induced phase transformation and grain growth of ti-6Al-4 V alloy. Int J Adv Manuf Technol 2016;87:859–66.
[26] Liu X.C, Zhang H.W, Lu K. Strain-induced ultrahard and ultrastable nanolaminated structure in nickel. Science 2013;342:337–40.
[27] Gao J.H, Jiang S, Zhang H, et al. Facile route to bulk ultrafine-grain steels for high strength and ductility. Nature 2021;590(7845):262–7.
[28] Liao Z, et al. Grain refinement mechanism of nickel-based superalloy by severe plastic deformation - mechanical machining case. Acta Mater 2019;180:2–14.
[29] Khan A.S, Zhang H, Takacs L. Mechanical response and modeling of fully compacted nanocrystalline iron and copper. Int J Plast 2000;16:1459–76.
[30] Khan A.S, Suh Y.S, Chen X, Takacs L, Zhang H. Nanocrystalline aluminum and iron: mechanical behavior at quasi-static and high strain rates, and constitutive modeling. Int J Plast 2006;22:195–209.
[31] Farrokh B, Khan A.S. Grain size, strain rate, and temperature dependence of flow stress in ultra-fine grained and nanocrystalline cu and Al: synthesis, experiment, and constitutive modeling. Int J Plast 2009;25:715–32.
[32] Yadav R, Chakladar N.D, Paul S. A dynamic recrystallization based constitutive flow model for micro-machining of ti-6Al-4V. J Manuf Process 2022;77:463–84.
[33] Jafarian F, Masoudi S, Umbrello D, Filice L. New strategies for improvement of numerical model accuracy in machining of nickel-based alloy. Simul Model Pract Theory 2019;94:134–48.
[34] Umbrello D, Bordin A, Imbrogno S, Bruschi S. 3D finite element modelling of surface modification in dry and cryogenic machining of EBM Ti6Al4V alloy. CIRP J Manuf Sci Technol 2017;18:92–100.
[35] Melkote S.N, Liu R, Fernandez-Zelaia P, Marusich T. A physically based constitutive model for simulation of segmented chip formation in orthogonal cutting of commercially pure titanium. CIRP Ann 2015;64:65–8.
[36] Imbrogno S, Rinaldi S, Umbrello D, Filice L, Franchi R, Del Prete A. A physically based constitutive model for predicting the surface integrity in machining of waspaloy. Mater Des 2018;152:140–55.
[37] Melkote S.N, Liu R, Fernandez-Zelaia P, Marusich T. A physically based constitutive model for simulation of segmented chip formation in orthogonal cutting of commercially pure titanium. CIRP Ann 2015;64:65–8.
[38] Bai W, Sun R, Leopold J, Silberschmidt V.V. Microstructural evolution of Ti6Al4V in ultrasonically assisted cutting: numerical modelling and experimental analysis. Ultrasonics 2017;78:70–82.
[39] Lin Y.C, Chen M, Zhong J. Effects of deformation temperatures on stress/strain distribution and microstructural evolution of deformed 42CrMo steel. Mater Des 2009;30:908–13.
[40] Lin Y.C, Chen X. A critical review of experimental results and constitutive descriptions for metals and alloys in hot working. Mater Des 2011;32:733–1759.
[41] Avrami M. Kinetics of phase change. II transformation-time relations for random distribution of nuclei. J Chem Phys 1940;8:212–24.
[42] Momeni A, Abbasi S.M. Effect of hot working on flow behavior of Ti–6Al–4V alloy in single phase and two phase regions. Mater Des 2010;31:3599–604.
[43] Johnson G.R, Cook W.H. Fracture characteristics of three metals subjected to various strains, strain rates, temperatures and pressures. Eng Fract Mech 1985;21: 31–48.
[44] Bai Y, Wierzbicki T. A new model of metal plasticity and fracture with pressure and lode dependence. Int J Plast 2008;24:1071–96.
[45] Johnson G.R. In: Strength and fracture characteristics of a titanium alloy (. 06al,. 04v) subjected to various strains, strain rates, temperatures and pressures. Naval Surface Weapons Center NSWC TR; 1985. p. 86–144.
[46] Chen G, Ren C, Yang X, Jin X, Guo T. Finite element simulation of high-speed machining of titanium alloy (Ti–6Al–4V) based on ductile failure model. Int J Adv Manuf Technol 2011;56:1027–38.
[47] Chen G, Ren C, Zhang P, Cui K, Li Y. Measurement and finite element simulation of micro-cutting temperatures of tool tip and workpiece. Int J Mach Tool Manuf 2013;75:16–26.
[48] Simo J.C, Hughes T.J. Computational inelasticity. Springer Science & Business Media; 2006.
[49] Chen G, James C, Chen S, Jawahir I. Machining-induced surface integrity in titanium alloy ti-6Al-4V: an investigation of cutting edge radius and cooling/ lubricating strategies. J Manuf Process 2022;353–64.
[50] Rinaldi S, Umbrello D, Melkote S.N. Modelling the effects of twinning and dislocation induced strengthening in orthogonal micro and macro cutting of commercially pure titanium. Int J Mech Sci 2021;190:106045.
[51] Hughes D.A, Korellis J.S. High load sliding, deformation microstructures, strength, and hardening for cutting and metal forming. Int J Mach Tool Manuf 2021;168:103766.